Appl. Phys. B (2013) 111:21–28
DOI 10.1007/s00340-012-5302-4

Applied Physics B
Lasers and Optics

A compact UHV package for microfabricated ion-trap arrays with direct electronic air-side access

Guido Wilpers · Patrick See · Patrick Gill · Alastair G. Sinclair

Received: 5 July 2012 / Accepted: 15 October 2012 / Published online: 9 February 2013
© Crown Copyright 2013

Abstract We have demonstrated a new apparatus for operating microfabricated ion-trap arrays in a compact ultra-high-vacuum setup with excellent optical and electrical access. The approach uses conventional components, materials and techniques in a unique fashion. The microtrap chip is mounted on a modified ceramic leadless chip carrier, the conductors of which serve as the vacuum feedthrough. The chip carrier is indium-sealed to stainless-steel components to form vacuum seals, resulting in short electrical path lengths of ≤20 mm from the trap electrodes under vacuum to air side. The feedthrough contains conductors for the radio-frequency trap drive, as well as 42 conductors for DC electrodes. Vacuum pressures of $\sim 1 \times 10^{-11}$ mbar are achieved, and ions have been confined and laser cooled in a microtrap chip. The apparatus enables accurate measurements of radio-frequency voltage amplitudes on the trap electrodes, yielding an excellent agreement between measured and modelled trap efficiencies. This feature is of significant use in establishing initial operation of new devices. The principle of the connectivity scheme presented here is applicable to larger ceramic chip carriers containing many more conductors.

1 Introduction

Quantum mechanical entanglement has moved from an exotic curiosity over the last 50 years into the realm of experimental physics with proof of principle demonstrations and first applications [1, 2]. Many experiments rely on the use of strings of ions trapped in linear segmented ion traps [3–8] and range from quantum computation [9–11] and quantum simulation [12] to quantum networking [13] and precision metrology [14, 15]. A strong trend towards miniaturisation, precision engineering on the micron level, and scalability taking advantage of microfabrication processes to produce "microtraps", has developed [6, 8, 16, 17].

Testing and characterisation of such ion traps is only possible under good ultra-high-vacuum (UHV) conditions [18, 19]. Setups require a combination of good optical access and multiple electrical feedthroughs for DC signals and high voltage RF. Most approaches up to now use standard and usually bulky UHV feedthroughs requiring considerable in-vacuum cabling and electronic filtering to be close to the trap electrodes [4, 20]. A widely used example [19, 21] adds a custom-made socket device enabling the use of ion traps packaged in pin grid array (PGA) carriers. This facilitates quick replacement of chips inside the vacuum.

All these approaches present limitations to properties desirable for ion-trap characterisation and operation. The desired properties include: (1) low-loss transmission of high-voltage RF signals, (2) transmission of low-noise DC voltages, (3) fast DC switching speeds, (4) efficient filtering of RF pick-up, and (5) flexibility of the electronic setup. An example for the need for flexibility is the difference between the electronic filtering for the measurement of anomalous heating rates [19, 22, 23] and for the fast and controlled shuttling of ions [5, 8, 24, 25].

Our new approach incorporates all these desired features. It presents a versatile and compact electronic UHV package for microtrap chips, combining the use of conventional parts and methods in a unique fashion. An indium-sealed commercial ceramic chip carrier forms a

G. Wilpers (✉) · P. See · P. Gill · A. G. Sinclair
National Physical Laboratory, Hampton Road,
Teddington, Middlesex TW11 0LW, UK
e-mail: guido.wilpers@npl.co.uk

compact multi-pin feedthrough without obstructing optical access. Air-side electronic access at 20 mm from the trap centre is achieved and filtering and cabling inside the vacuum can be completely avoided. The principle of the approach is inherently scalable to some 200 DC contacts using commercially available chip carriers. The completed electronic package can withstand rigorous cleaning and rapid cycling to high temperatures. This makes it entirely suitable for use in a UHV environment.

In principle, the desired features enumerated above are also addressed in an approach by Kaufmann et al. [26]. It relies on a custom-made component, which is milled from an alumina block and uses thick-film technology for electrical conductors.

We have demonstrated the performance of our package by testing and successfully operating our new 3D, monolithic microfabricated ion trap [27, 28]. We measured and calibrated radio-frequency voltage amplitudes on the RF electrodes, U_{rf}, enabling us to accurately set the experimental trap parameters based on the knowledge gained from ion-trap simulations [27]. Subsequently, loading into the new trap was greatly simplified and the demonstration of the excellent agreement between measured [28] and modelled trap parameters was made possible. Finally, measurements of background-gas collisions with trapped ions allowed us to confirm the vacuum pressure achieved.

This paper is organised as follows. In Sect. 2 we describe the assembly of the new package, separately describing the electronic part in Sect. 2.1 and the UHV part in Sects. 2.2 and 2.3. In Sect. 3 we summarise the aspects of the experimental setup relevant to the tests carried out. In Sect. 4 we present measurements demonstrating the performance and versatility of the package in operation. Section 5 concludes the paper.

2 Apparatus

Intricate wafer-based electronic circuits are mounted in robust electronic packages for ease of handling and for standardisation of connectivity. In addition, microtrap packaging needs to provide good optical access and UHV conditions. We incorporate these features into our design using a conventional ceramic leadless chip carrier (LCC, see Fig. 1) that is attached to a UHV chamber with cold-welded indium seals (Fig. 2). In this way we realise an ultra-compact multi-contact feedthrough including the microtrap chip with 42 DC contacts and RF connectivity along the edges of a 3 cm × 3 cm area. We achieve access from the air side to the trap centre with path lengths of 20 mm or less, and avoid any cabling or electronic filtering inside the vacuum. At the same time we maximise optical access with a total solid angle of $\sim 1.4\pi$ sr. The principle of the system could easily

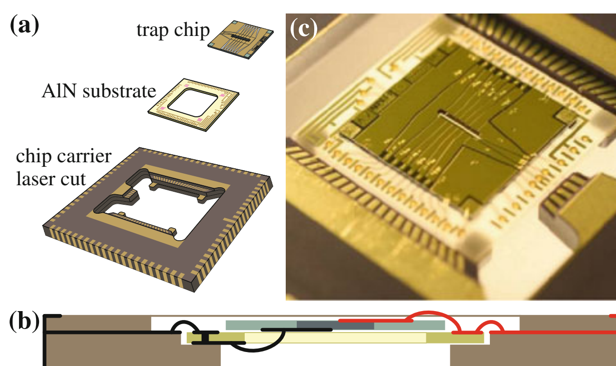

Fig. 1 Electronic package, looking at the front-side surface. **a** Exploded view of the sandwiched package (RF contacts on the *left*). **b** Cross-section through package indicating paths connecting trap electrodes to LCC contacts; *left* from back-side surface of chip along AlN substrate with via to LCC; *right* from front-side surface of chip along AlN substrate to LCC. **c** Photo of inner part of completed package (glued and wirebonded) with working microtrap chip. RF contacts are on the *right*

be applied to other commercially available ceramic chip carriers enabling up to 200 DC contacts. This provides a route for packaging more complex microtrap devices.

2.1 Electronic package

In our present setup we use a conventional 84-pin alumina LCC containing gold-plated tracks for electronic packaging (Fig. 1). Water-jet-guided laser cutting opens a through hole in the central part of the carrier. The method achieves a smooth and clean vertical cut through the 2.2-mm-thick alumina. The cut opens up orifices for optical access and vacuum conductivity through the LCC (Sect. 2.2). Four small ledges are left to support the chip package. Connections to DC electrodes are made along opposite edges of the LCC (21 connections per edge). A third edge facilitates connections to the RF electrodes. This reflects the layout of our microtrap chip [28]. The chip is also double-sided, i.e. it contains electrodes on front- and back-side surfaces of the chip. To connect them all to the single-sided chip carrier we sandwich a double-sided aluminium-nitride (AlN) substrate containing electrical vias between microtrap chip and LCC. The sandwiched stack is bonded together using a heat curing epoxy (Epotek H77), with the connection strong enough to survive repeated wirebonding on both sides. We avoid thermal stress in the completed package due to differences in the coefficients of thermal expansion (CTE) in two ways. First, the use of AlN allows us to bridge the difference between the CTE of the silicon bulk of the ion-trap chip, and the alumina of the LCC. Second, we bond only with ~ 1 mm^2 patches applied at the corners of the chip and AlN substrate. In this way the high CTE of the epoxy cannot cause the thermal stress that

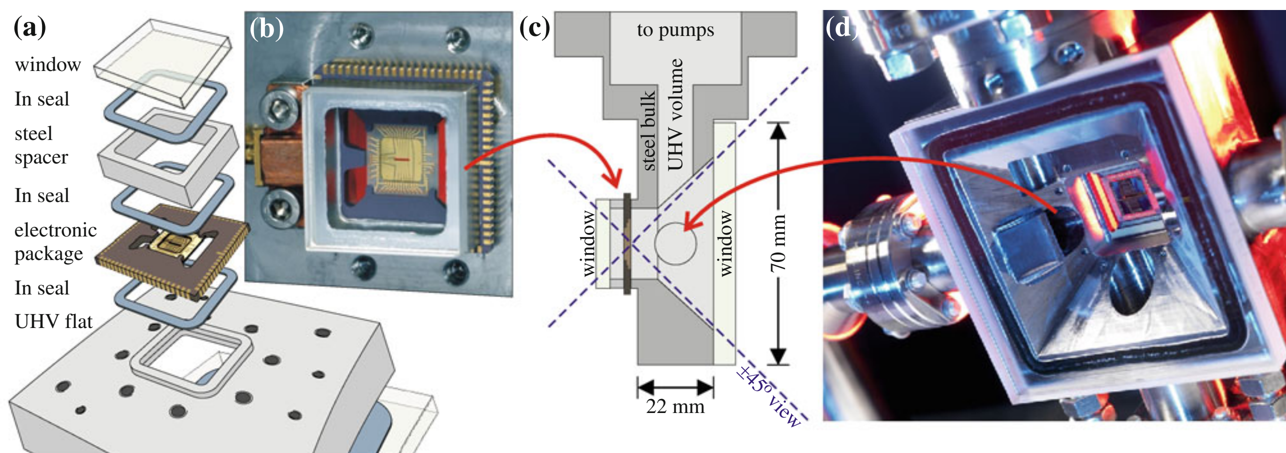

Fig. 2 Details of the UHV packaging (see text; "front-/back-side surface" as defined in Fig. 1). **a** Exploded view of the stack containing the electronic package, window (25.6 × 25.6 × 4 mm^3), steel spacer (8 mm high) and three indium seals, attached to the UHV flat. **b** Photograph of the assembled stack with air-side LCC contacts and excellent optical access. On the *left side* the RF connector is attached. **c** Cross-section of the stack with the UHV flat (vertical centre cut). The electronic package is attached on the *left side* and the 70 mm × 70 mm × 7 mm window on the right. This window is also indium sealed to the UHV flat. A 10 mm-wide and 35 mm-deep conduit leads from the centre to a DN40 CF flange for connection to the vacuum pumps. The ring in the centre indicates a hole (12 mm diameter) with DN16 CF port containing an atom source [29] with a hotplate of ~1 cm^2 area, coated with strontium from a small oven. **d** View through the 70 mm window showing the excellent optical access to the microtrap, visible at the back. On the *left* a thin metal shield partly covers the hole containing the atom source

continuous bonding along the length of the substrates could result in. Altogether, the completed electronic package can withstand wide and rapid temperature cycles tested up to 280 °C. The electronic package is robust, fully UHV compatible and able to withstand rigorous cleaning. This includes the use of normal cleaning solvents and mild acids as well as oxygen-plasma ashing at high power.

2.2 Vacuum package

The requirements for the UHV package (Fig. 2) comprise: (1) straightforward and flexible electronic access to the trap electrodes, (2) a pressure $\leq 10^{-10}$ mbar at the ions, and (3) excellent optical access.

To ensure straightforward air-side electronic access we attach the front-side surface of the LCC to a small ledge (2.6 mm wide and standing proud by 2 mm) on the face of the stainless-steel vacuum chamber (Fig. 2a). We complete the vacuum volume by attaching a small steel spacer and an optical flat to the back-side surface of the LCC. For UHV sealing we use 0.5-mm diameter indium wire and fit three such gaskets between the window, steel spacer, insulating surfaces of the LCC and the vacuum system. Applying high pressure to the stacked components, we achieve a cold-welded bond of the indium to all surfaces. The indium seals (2.6 mm wide, $<100\,\mu$m high) bond the stack firmly together without the need for permanent clamping. We leave 0.5 mm of insulating space between the weld and the electrical contacts, sufficient to apply a RF amplitude up to 700 V without surface flashover or electrical breakdown in air. The completed package (Fig. 2b) yields a miniature multi-pin electronic feedthrough for UHV, and access to the trap centre from the air side with a path length of ≤20 mm.

To achieve sufficient vacuum conductivity, the steel spacer provides a spacing of at least 4 mm between the microtrap's surface and the window. This keeps the vacuum conductivity from the centre of the small volume through the LCC's laser-cut orifices to the main chamber above 5 l/s. Presently, we use an 8 mm separation, i.e. ~30 times the ion-electrode distance in the microtrap. This allows us to minimise the effect of stray charges without the use of a conductive coating on the window [30].

Vacuum conductivity also prescribes the layout of the "UHV flat" (Fig. 2c), a custom-made stainless-steel cuboid on a DN40 ConFlat (CF) flange to which the electronic package is attached. The requirements for optical access and for mechanical rigidity further affect the geometry. A 10-mm wide conduit, connecting to a DN40 CF cube with 20 l/s ion pump, non-evaporable getter, ion gauge and all-metal valve, yields ~20 l/s conductivity. A minimum thickness of the walls of 6 mm enables us to apply the forces necessary for cold welding of indium. An indium-sealed window opposite the LCC enables an unhindered view through the trap (Fig. 2d). The use of cold-welded indium allows us to avoid any build-up of mechanical stress, even during bake-out. Thus, the optical performance of the anti-reflection coated, high-quality fused silica we use is not compromised. The window layout enables optical access to the microtrap centre corresponding to solid angles of 0.7π sr from each side of the trap. The range of possible viewing angles in the plane

normal to the microtrap's z-axis is indicated in Fig. 2c) by the "±45° view". It is worth noting that the thin electrodes of our microtrap [28] enable optical access to the ion with a corresponding range of ±43°.

2.3 Vacuum processing

To overcome limitations due to the low melting point of indium (∼156 °C) we follow a procedure with two bake-out stages, enabling us to reach a UHV pressure of $\sim 1 \times 10^{-11}$ mbar.

To prepare a new sytem from scratch, we first bake all parts inside a turbo-pumped UHV chamber at up to 240 °C for 48 h. Secondly, we assemble the complete system with all indium seals within 8 h. This is done in air under a clean-air flow hood to avoid any contamination with dust particles. Thirdly, we run the final UHV bake of the assembled system at 130 °C for another 48 h. In this step we also activate the non-evaporable getter.

3 Experimental setup

Details on the wider experimental apparatus can be found elsewhere [28, 29, 31]. Here we only summarise the parts relevant to the results presented in this paper.

We supply high-voltage RF to the trap via a short (∼7 cm) coaxial cable connected to the high-voltage end of a helical resonator [32], see Fig. 3. We couple up to 1 W of power from a synthesizer and amplifier using a seed coil impedance-matched to the resonator. The loaded resonance is typically set at 18 MHz with a quality factor $Q = 155$.

We load the ion trap using a doubly resonant photo-ionisation process [29]. We Doppler cool trapped ions on the 5s $^2S_{1/2}$–5p $^2P_{1/2}$ transition at 422 nm ($\Gamma/2\pi \approx 20$ MHz). For continuous cooling and detection we use a de-tuning of 12 MHz below resonance and an intensity of half the saturation level.

We detect fluorescence from the cooling transition of trapped ions in either of the two ways. On each side of the trap an objective lens (NA ∼ 0.43, magnification typically set to 10) images the ions onto single-photon counting devices: a photomultiplier on one side and an electron-multiplying CCD camera on the opposite side (24 μm pixel size). The optical axis of the detection setup is normal to and centered on both vacuum windows. Each objective lens covers $\sim 0.25\pi$ sr of the $\sim 0.7\pi$ sr total optical access on its side.

To measure the motional frequencies of a single trapped ion we used either of the following two methods. In one we utilise resonant heating of the ion's motion with RF voltages applied to DC electrodes during Doppler cooling. Here, tuning the frequency to one of the ion's motional resonances heats the ion, and reduces fluorescence due to Doppler broadening. The other method utilises frequency-resolved spectroscopy on the narrow qubit transition, 5s $^2S_{1/2}$–4d $^2D_{5/2}$ with a natural linewidth of 0.4 Hz [33] at 674 nm. For the measurement of the excitation probabilities we use the electron shelving technique with fluorescence on the Doppler cooling transition.

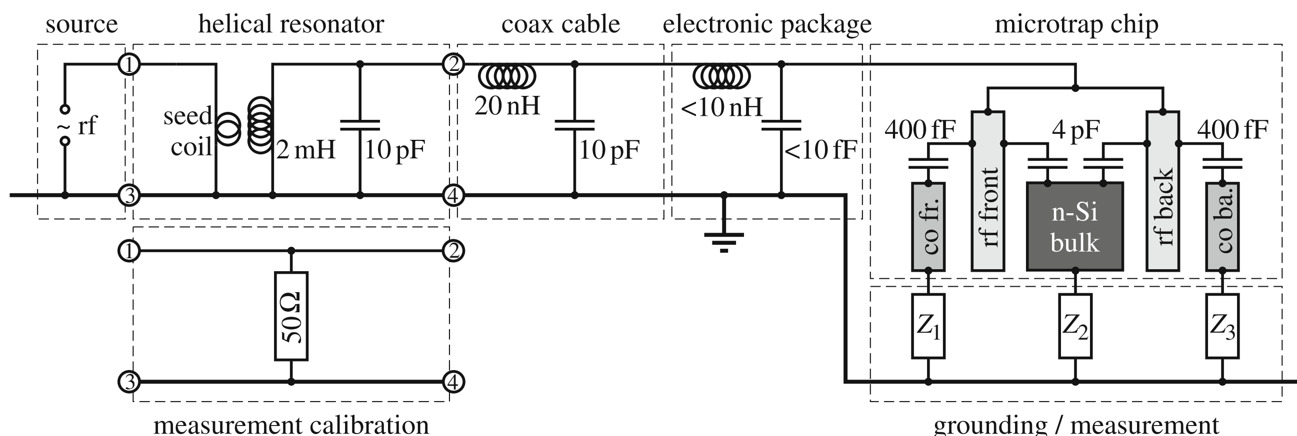

Fig. 3 Schematic setup for the high-voltage radio-frequency circuit. Values are rough estimates for indication only. For normal operation up to 1 W of RF power is fed with an impedance-matched seed coil into a helical resonator. Its output is connected to the chip carrier via a short coaxial cable (∼7 cm). Inside the electronic package wirebonds connect to all the microtrap electrodes (shown for RF only). On the microtrap chip [28] capacitive coupling through a silicon dioxide layer connects the RF electrodes to a set of compensation electrodes (co fr.) on the front-side surface of the chip (∼400 fF) and similarly on the back-side surface (co ba.). Both RF electrodes also couple to the silicon bulk of the chip with a total of ∼4 pF. All DC electrodes and the n-doped silicon bulk are kept at RF ground with filters fitted on the air side indicated by the impedances Z_1, Z_2 and Z_3. These include the fixed electronic packaging contributions similar to the shown RF values. On the air side each of those can be replaced by a low impedance (≤50 Ω) circuit to measure RF pick-up. For calibration purposes the helical resonator and seed coil can be replaced by a parallel 50 Ω resistor connecting to positions 1, 2, 3, and 4 as indicated

4 Results

We have used our package to aid the development and testing of microtrap chips conceived and produced in our group [27, 28]. To demonstrate the performance of the package we present some of the results.

4.1 Calibrated measurements of RF amplitudes

A common problem for initial loading of ions into a new trap is the lack of knowledge of the exact RF-voltage amplitude, U_{rf}, present at the trap electodes. With amplitudes of several hundred volts needed, resonant build-up circuits are normally employed. Cabling, vacuum feedthroughs and the ion trap necessarily have to be connected, thus substantially shifting the basic resonator properties. Fig. 3 shows the main sources of reactance of the resonator and trap setup for our case. Even the short coaxial cable and the small microtrap chip add parallel capacitances of the same magnitude as that of the helical resonator, while the serial inductive reactances are much smaller. In these more complicated circuits with distributed capacitances and inductances, estimating the resulting U_{rf} can be difficult. The direct access and short lines to the microtrap electrodes in our setup add negligible inductive reactances. This allows us to measure U_{rf} directly in a calibrated fashion.

The low capacitive coupling of the RF electrodes to DC electrodes and the n-doped highly conductive silicon bulk separates the resonant circuit from the grounded electrodes (Fig. 3, $Z_{1,2,3} \rightarrow 0$) to a high degree. With capacitances of 4 pF and smaller, reactances $\gg$1kΩ are achieved for typical drive frequencies up to 40 MHz. Introducing a measurement circuit with low impedance ($Z_{1,2,3} \leq 50\,\Omega$) between DC electrodes and ground presents a negligible disturbance to the resonant circuit and allows us to measure the low-voltage RF pick-up on the DC electrodes and the silicon bulk. In fact, checking the impedance matching of the input power for the different setups, we find that the relative changes of the resonant frequency are $<2 \times 10^{-3}$. On resonance, reflections remain at least 45 dB below the input power, and the quality factor of $\sim$155 remains unchanged.

To calibrate the measurements, we need to know the attenuation of the measured pick-up signal relative to U_{rf}. For this purpose we replace the resonant circuit, namely the helical resonator with its seed coil, by a 50 Ω resistive load connected in parallel to the RF electrodes (see "measurement calibration" module in Fig. 3). We apply a RF signal with a known voltage amplitude across the load. The low reactance ($\leq 1\,\Omega$) between the resistor and the RF electrodes due to the low serial inductance (≤20 nH) of the short coaxial cable and the wirebonds leads to negligible change of the RF-voltage amplitude on the RF electrode, U_{rf}, compared to the 50 Ω resistor. Thus, we can assume the voltage amplitudes to be equal to within ±1 % up to 40 MHz.

With the calibration completed, we measured the actual U_{rf} with the helical resonator in place for scans across the resonance at 18 MHz. Fig. 4 shows the results deduced from three different pick-up measurements. We find very good agreement between these calibrated signals. The lineshapes show quality factors of $Q = 155 \pm 1$ and follow closely the behaviour expected for a series LCR circuit. The peak voltages agree to within ±3 %. We measured U_{rf} on resonance up to 330 V, and find the expected square-root dependence on the applied input power. We find higher harmonics measured up to the 6th order to be at least 76 dB down in power.

4.2 Comparison to trap model

Finite element modelling has been used [27] to determine the best value of U_{rf} for optimal trap performance. The calibrated measurements of U_{rf} enable the desired value to

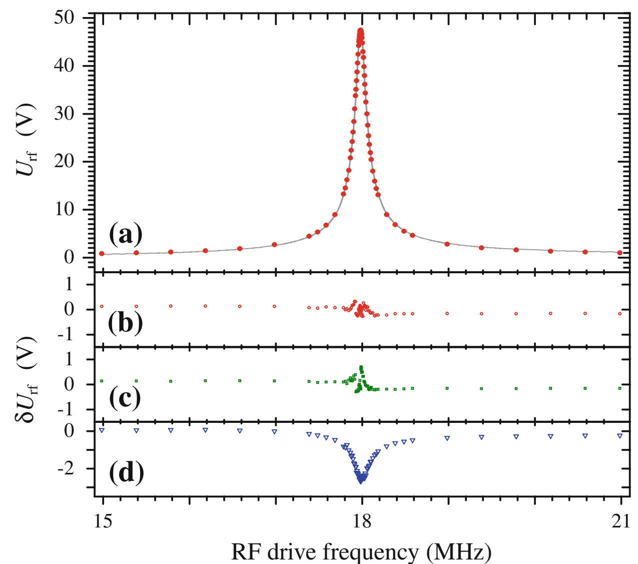

Fig. 4 Comparison of resonant RF-voltage amplitude U_{rf} as determined by capacitive coupling using three different pick-up schemes. **a** Calibrated U_{rf} versus RF frequency, measured using font-side compensation electrodes ($\sim$0.4 pF) coupling to sense the RF signal (*points*). The impedance of the measurement setup was $\sim 110\,\Omega$. The fit, $U_{rf,fit}$ (*line*), assumes a voltage drop across the capacitance in a series LCR circuit. **b** Residual deviations from the fit, $\delta U_{rf} = U_{rf,data} - U_{rf,fit}$, for the data of **a**. Using the fit of **a** as a reference, this first measurement is compared to two other approaches. Residual deviations are presented for U_{rf} measured by capacitively coupling via **c** backside compensation electrodes, and **d** the n-Si bulk with $\sim$4 pF coupling, and a $\sim 2\,\Omega$ connection to ground. The resonance frequencies for the measurements all agree to within ± 1 kHz and the linewidths are (116 ± 1) kHz. The larger deviation in d) is attributed to the calibration uncertainty

be applied accurately. With this combined knowledge, we remove the greatest unknown in establishing operation of a new trap device.

We characterised the trap performance with measurements of motional frequencies. Knowing U_{rf} an efficiency parameter, ε, can be deduced. It is a measure of how much the effect of U_{rf} in producing a pseudopotential is reduced for a given electrode geometry compared to that of an ideal trap with hyperbolic trap electrodes and the same ion-electrode distance, d_0. The efficiency parameter is defined as [34]

$$\varepsilon = \frac{\sqrt{2}\omega_r M \Omega_{rf} {d_0}^2}{e U_{rf}}, \quad (1)$$

where ω_r is the angular motional frequency, M the ion mass, e the electrical charge, and Ω_{rf} the trap-drive angular frequency. Eq. 1 holds for negligible influence of endcap voltages providing axial confinement. For an ideal hyperbolic geometry $\varepsilon = 1$.

We measured motional frequencies with frequency-resolved spectroscopy of the carrier and motional sidebands on the narrow quadrupole transition, and with resonant heating of the ion's motion with RF voltages. Based on 10 measurement results over a wide range of parameter settings we found $\varepsilon_{exp} = 0.72 \pm 0.03$ [28]. We find excellent agreement with the expected efficiency $\varepsilon_{FEM} = 0.71 \pm 0.01$, calculated using finite element modelling [27]. This demonstrates that the measurement procedure of Sect. 4.1 is an easy and reliable technique for calibrating U_{rf}.

4.3 Vacuum performance

We have trapped and continuously cooled single ions and pairs of ions, see Fig. 5, with times in excess of 24 and 5 h, respectively.

We measured background-gas collisions with a trapped ion to estimate the UHV pressure at the position of the ion. For this we recorded dropouts of the cooling fluorescence assumed to be due to energetic elastic collisions of molecules with the ion leading to substantial kinetic energy gain. Due to Doppler shifts, fluorescence is suppressed for a short while before the ion is cooled down again. During recooling the fluorescence gradually recovers as described by a model given in [35]. For the final cooling stages we assumed approximately exponential behaviour of the fluorescence recovery. Our setup limited detectable dropouts to minimum recovery time constants of 50 ms, corresponding to a minimum energy transfer of 10 meV in a collision. We estimated collision rates following a quasi-classical approach used in [18] and [36] for the collision of a thermalised partial gas of neutral molecules (of static electric polarisability α) with a localised ion (of charge e). We assumed the molecules to be scattered in the

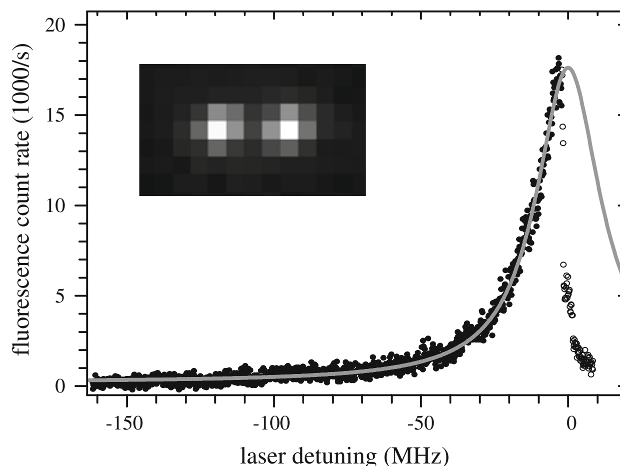

Fig. 5 Examples of Doppler cooled $^{88}Sr^+$ ions. The inset shows an image of cooling fluorescence from a pair of ions separated by $\sim 18\,\mu$m. In this example we used a magnification of 5 for imaging onto the CCD camera. The graph shows the fluorescence count rate from a single ion in a 422 nm laser frequency scan across the resonance with power set to ~ 0.6 of saturation intensity (*points* and *circles*). The *solid line* is a fit of a Lorentzian line shape to the *solid points*, i.e. for detuning below resonance, with a full width at half maximum of 26.5 MHz. The natural line width is $\sim$ 20.2 MHz. Note, that we ignore the effect of the repumper here. Above resonance the ion is heated up and fluorescence lost (*open circles*)

polarisation-dependent central force field of the ion, leading to a potential $V(r) = -\alpha e^2/(8\pi\epsilon_0 r^4)$, where r is the ion-molecule separation. The elastic collisional cross section $\sigma_{el} \approx 2.7\pi\sqrt{\alpha e^2/(16\epsilon_0\hbar v)}^3$, where v is the impact velocity. When calculating the averaged collisional scattering rate for each partial gas, we took this dependence into account by integrating over the velocity distribution. We included the effect of the minimum detectable energy transfer by starting the integration for each molecule at the impact velocity corresponding to an average energy transfer of 10 meV. We found that for the lightest molecules the detectable scattering rate can be substantially reduced. We expect it to be dominated by H_2O, CO or N_2, O_2 and CO_2 instead. Residual gas analysis enabled us to estimate relative partial pressures and we included these in deriving the total pressure from detected collision rates. We used values for α from [37] and [38]. With 300 dropouts detected we found an average time between collisions of (750 $\pm$ 50) s and estimated the pressure to be close to 2×10^{-11} mbar.

Notably, after recharging the 1 cm^2 sized atomic source hotplate with strontium [29], we observed a further reduced collision rate with (2,400 $\pm$ 700) s between collisions based on 13 events, corresponding to a pressure of less than 1×10^{-11} mbar. The fresh strontium obviously acted as active getter material and appears to have more than doubled the effect of the UHV pumps. This indicates that a

miniaturised UHV system with a small surface area only using small pumps close to the microtrap might well achieve a similar UHV performance.

5 Conclusions and outlook

We have demonstrated a new approach for testing and operating microtraps in a compact and electronically flexible UHV setup, including excellent optical access with a total solid angle of $\sim 1.4\pi\,\mathrm{sr}$.

The approach relies entirely on conventional materials easily adapted for the purpose, in particular the use of ceramic chip carriers with indium sealing. We have realised a compact multi-pin feedthrough, including RF and 42 DC contacts, with air-side electrical access to within 20 mm of the trap centre. We have demonstrated operation of the package with laser-cooled ions in a newly designed and microfabricated trap. We verified UHV performance at the position of the ions with the help of background-gas collision measurements to reach below 1×10^{-11} mbar. We have substantiated the electronic versatility of the package by accurate measurements of RF-voltage amplitudes in the trap achieved with negligible perturbation to the resonant RF setup. Knowledge of the RF-voltage amplitude enabled us in turn to set trap parameters accurately in combination with numerical simulations of the trap's pseudopotential. This greatly simplified the loading of ions into the new trap and allowed us to prove the excellent agreement between measured and modelled trap efficiencies.

Potential improvements include replacing the nickel adhesion layer used in the chip carriers with titanium to achieve a fully non-magnetic environment. The sealing approach and chamber design can be transferred to other commercially available ceramic chip carriers, e.g. PGAs. Up to 200 contacts could easily be realised this way. Markedly higher numbers could be achieved with modified versions to provide full scalability for microfabricated ion-trap operation. In addition, miniaturisation of the UHV system could be achieved. The more than twofold improved pressure with the getter effect of the small hotplate, freshly loaded with strontium atoms, suggests the possibility to achieve excellent UHV performance with miniaturised getters and ion pumps only.

Acknowledgments We thank Dirk Kähler (Fraunhofer ISIT) for help with the electronic packaging. We thank Mark Oxborrow (NPL), Tanja Mehlstäubler (PTB) and Daniel Stick (Sandia National Labs) for helpful discussions. This work was supported by NPL's strategic research programme, the UK NMO Pathfinder programme, and by EU contracts IST 2005-15714-SCALA, and IST 2006-517675-MICROTRAP.

References

1. C. Monroe, Nature. **416**, 238 (2002)
2. T.D. Ladd, F. Jelezko, R. Laflamme, Y. Nakamura, C. Monroe, J.L. O'Brien, Nature. **464**, 45 (2010)
3. M.D. Barrett, J. Chiaverini, T. Schaetz, J. Britton, W.M. Itano, J.D. Jost, E. Knill, C. Langer, D. Leibfried, R. Ozeri, D.J. Wineland, Nature. **429**, 737 (2004)
4. S.A. Schulz, U. Poschinger, F. Ziesel, F. Schmidt-Kaler, New J. Phys. **10**, 045007 (2008)
5. R.B. Blakestad, C. Ospelkaus, A.P. VanDevender, J.H. Wesenberg, M.J. Biercuk, D. Leibfried, D.J. Wineland, Phys. Rev. A **84**, 032314 (2011)
6. S. Seidelin, J. Chiaverini, R. Reichle, J.J. Bollinger, D. Leibfried, J. Britton, J.H. Wesenberg, R.B. Blakestad, R.J. Epstein, D.B. Hume, W.M. Itano, J.D. Jost, C. Langer, R. Ozeri, N. Shiga, D.J. Wineland, Phys. Rev. Lett. **96**, 253003 (2006)
7. J. Labaziewicz, Y. Ge, P. Antohi, D. Leibrandt, K.R. Brown, I.L. Chuang, Phys. Rev. Lett. **100**, 013001 (2008)
8. D.L. Moehring, C. Highstrete, D. Stick, K.M. Fortier, R. Haltli, C. Tigges, M.G. Blain, New J. Phys. **13**, 075018 (2011)
9. R. Blatt, D. Wineland, Nature. **453**, 1008 (2008)
10. J.P. Home, D. Hanneke, J.D. Jost, J.M. Amini, D. Leibfried, D.J. Wineland, Science. **325**, 1227 (2009)
11. D. Hanneke, J.P. Home, J.D. Jost, J.M. Amini, D. Leibfried, D.J. Wineland, Nat. Phys. **6**, 13 (2010)
12. R. Blatt, C.F. Roos, Nat. Phys. **8**, 277 (2012)
13. D.L. Moehring, P. Maunz, S. Olmschenk, K.C. Younge, D.N. Matsukevich, L.-M. Duan, C. Monroe, Nature. **449**, 68 (2007)
14. C.F. Roos, M. Chwalla, K. Kim, M. Riebe, R. Blatt, Nature. **443**, 316 (2006)
15. T. Rosenband, D.B. Hume, P.O. Schmidt, C.W. Chou, A. Brusch, L. Lorini, W.H. Oskay, R.E. Drullinger, T.M. Fortier, J.E. Stalnaker, S.A. Diddams, W.C. Swann, N.R. Newbury, W.M. Itano, D.J. Wineland, J.C. Bergquist, Science. **319**, 1808 (2008)
16. D. Stick, W.K. Hensinger, S. Olmschenk, M.J. Madsen, K. Schwab, C. Monroe, Nat. Phys. **2**, 36 (2006)
17. J. Britton, D. Leibfried, J.A. Beall, R.B. Blakestad, J.H. Wesenberg, D.J. Wineland, Appl. Phys. Lett. **95**, 173102 (2009)
18. D.J. Wineland, C. Monroe, W.M. Itano, D. Leibfried, B.E. King, D.M. Meekhof, J. Res. Natl. Inst. Stand. Technol. **103**, 259 (1998)
19. D.T.C. Allcock, J.A. Sherman, D.N. Stacey, A.H. Burrell, J.M. Curtis, G. Imreh, N.M. Linke, D.J. Szwer, S.C. Webster, A.M Steane, D.M. Lucas, New J. Phys. **12**, 053026 (2010)
20. W.K. Hensinger, S. Olmschenk, D. Stick, D. Hucul, M. Yeo, M. Acton, L. Deslauriers, C. Monroe, J. Rabchuk, Appl. Phys. Lett. **88**, 034101 (2006)
21. J.J. McLoughlin, A.H. Nizamani, J.D. Siverns, R.C. Sterling, M.D. Hughes, B. Lekitsch, B. Stein, S. Weidt, W.K. Hensinger, Phys. Rev. A **83**, 013406 (2011)
22. Q.A. Turchette, D. Kielpinski, B.E. King, D. Leibfried, D.M. Meekhof, C.J. Myatt, M.A. Rowe, C.A. Sackett, C.S. Wood, W.M. Itano, C. Monroe, D.J. Wineland, Phys. Rev. A **61**, 063418 (2000)
23. N. Daniilidis, S. Narayanan, S.A. Möller, R. Clark, T.E. Lee, P.J. Leek, A. Wallraff, S. Schulz, F. Schmidt-Kaler, H. Häffner, New J. Phys. **13**, 013032 (2011)
24. A. Walther, F. Ziesel, T. Ruster, S.T. Dawkins, K. Ott, M. Hettrich, K. Singer, F. Schmidt-Kaler, U. Poschinger, Phys. Rev. Lett. **109**, 080501 (2012)
25. R. Bowler, J. Gaebler, Y. Lin, T.R. Tan, D. Hanneke, J.D. Jost, J.P. Home, D. Leibfried, D.J. Wineland, Phys. Rev. Lett. **109**, 080502 (2012)
26. D. Kaufmann, T. Collath, M. Baig, P. Kaufmann, E. Asenwar, M. Johanning, C. Wunderlich, Appl. Phys. B. **107**, 935–943 (2012)

27. M. Brownnutt, G. Wilpers, P. Gill, R.C. Thompson, A.G. Sinclair, New J. Phys. **8**, 232 (2006)
28. G. Wilpers, P. See, P. Gill, A.G. Sinclair, Nat. Nanotech. **7**, 572–576 (2012)
29. M. Brownnutt, V. Letchumanan, G. Wilpers, R.C. Thompson, P. Gill, A.G. Sinclair, Appl. Phys. B. **87**, 411 (2007)
30. M. Harlander, M. Brownnutt, W. Hänsel, R. Blatt, New J. Phys. **12**, 093035 (2010)
31. V. Letchumanan, P. Gill, E. Riis, A.G. Sinclair, Phys. Rev. A. **70**, 033419 (2004)
32. W.W. Macalpine, R.O. Schildknecht, in Proceedings of the IRE, 2099 (1959)
33. V. Letchumanan, M.A. Wilson, P. Gill, A.G. Sinclair, Phys. Rev. A. **72**, 012509 (2005)
34. M.J. Madsen, W.K. Hensinger, D. Stick, J.A. Rabchuk, C. Monroe, Appl. Phys. B **78**, 639 (2004)
35. J.H. Wesenberg, R.J. Epstein, D. Leibfried, R.B. Blakestad, J. Britton, J.P. Home, W.M. Itano, J.D. Jost, E. Knill, C. Langer, R. Ozeri, S. Seidelin, D.J. Wineland, Phys. Rev. A **76**, 053416 (2007)
36. L.D. Landau, E.M. Lifshitz, *Course of theoretical physics - volume 3, quantum mechanics (non-relativistic theory)* (Pergamon Press Ltd, Oxford, 1977)
37. J.B. Hasted, *Physics of atomic collisions* (Butterworth & Co. (Publishers) Ltd, London, 1964)
38. H.-J. Werner, W. Meyer, Phys. Rev. A **13**, 13–16 (1976)